Renewable Energy 220 (2024) 119722

Contents lists available at ScienceDirect

Renewable Energy

journal homepage: www.elsevier.com/locate/renene

Validation of model chains for global tilted irradiance on East-West vertical bifacial photovoltaics at high latitudes

Mattia Manni [a,*], Sami Jouttijärvi [b], Samuli Ranta [c], Kati Miettunen [b], Gabriele Lobaccaro [a]

[a] Department of Civil and Environmental Engineering, Faculty of Engineering, Norwegian University of Science and Technology (NTNU), 7491, Trondheim, Norway
[b] Department of Mechanical and Materials Engineering, Faculty of Technology, University of Turku, Vesilinnantie 5, 20500, Turku, Finland
[c] New Energy Research Group, Turku University of Applied Sciences (TUAS), Joukahaisenkatu 7, 20520, Turku, Finland

ARTICLE INFO

Keywords:
Decomposition modelling
Transposition modelling
Solar irradiance
Photovoltaics
Error analysis
Nordics conditions

ABSTRACT

In this paper, a methodology is introduced to identify and validate the most effective model chain to estimate solar irradiance on East-West vertical bifacial photovoltaics (E-W VBPV) at high latitudes. While previous studies mainly focused on the validation of a specific step of the model chain (i.e., decomposition or transposition stage), this work investigates the whole model chain and how the combination of different models influences the results' accuracy. After a comprehensive review, the 29 decomposition models, which perform the best in the Nordics, and the 25 most common physical and empirical transposition models are selected and combined into 725 model chains. Each model chain is experimentally validated against 1-min data about global tilted irradiance on the front and the rear of E-W VBPV in Turku (Finland). Nine different statistical metrics are calculated to rank the model chains while describing various aspects of the model chain performance (e.g., error magnitude, bias direction, reference data fitting). The main research outcomes indicate that the accuracy and bias of the model chains differ between the East and West sides of the VBPV. Therefore, using a specific model chain for each VBPV side is recommended. In this regard, the Erbs/Steven1 (decomposition model/transposition model) model chain is the top-ranked for the East side, while the Yang2/Hay1 model chain results the best for the West side. Following this, recommendations to select appropriate solar irradiance model chains for future E-W VBPV applications at high latitudes are outlined.

1. Introduction

Rising global energy consumption [1] requires increasing renewable energy production [2] to reach net zero emissions by 2050, while ensuring reliable energy supply. Since energy consumption in buildings is a significant source of greenhouse gas emissions (GHG), reducing the carbon footprint of the built environment is crucial. The report of the Intergovernmental Panel on Climate Change [3] has identified solar energy together with wind energy as the energy sources that are expected to contribute the most to the decarbonization of the energy sector. Within this framework, exploiting solar photovoltaic (PV) panels represents an essential strategy due to the scalability of the PV modules, which can be used both in utility-scale power plants (urban scale) and in kilowatt-scale small production (building scale). Thus, reducing GHG from the built environment by satisfying the energy consumption of buildings with PV electricity produced at the spot with building-integrated panels and rooftop installations can advance the transition towards net zero emission targets.

In this framework, the deployment of bifacial PV (BPV) panels, capable of harnessing sunlight from both sides (i.e., front and rear side), is gaining interest compared to traditional monofacial PV (MPV) panels, opening new possibilities for solar energy generation and applications (i.e., vertical mounted PV in agriculture, landscape, and building applications). Differently from tilted and Equator-facing MPV installations, which typically achieve peak production at noon, vertical BPV (VBPV) panels with sides facing East and West (E-W) show two production peaks, one early in the morning and another late in the afternoon [4,5], aligning with the electricity demand patterns observed in a typical residential building (i.e., peaks around 7–8 a.m. and 5–6 p.m [6]). This characteristic of the E-W VBPV facilitates increased self-consumption of PV electricity. When it comes to high-latitude locations [4] characterized by significant annual variations in solar irradiation, low solar elevation, and high albedo due to the presence of snow deposits on the ground [5,7], VBPV emerges as a suitable solution outperforming optimally oriented MPV installations [8,9].

* Corresponding author.
E-mail address: mattia.manni@ntnu.no (M. Manni).

https://doi.org/10.1016/j.renene.2023.119722
Received 14 July 2023; Received in revised form 8 November 2023; Accepted 22 November 2023
Available online 26 November 2023

List of abbreviations including units and nomenclature

Variables

AIC	Akaike information criterion [W m^{-2}]
AST	Apparent solar time [0–24]
BIC	Bayesian information criterion [W m^{-2}]
CPI	Combined performance index [W m^{-2}]
E	Solar irradiance [W m^{-2}]
K_{CSI}	Clear-sky index for global horizontal irradiance [dimensionless]
k_t	Clearness index [dimensionless]
KSI	Kolmogorov–Smirnov test integral [W m^{-2}]
MAD	Mean absolute deviation [W m^{-2}]
MBD	Mean biased deviation [W m^{-2}]
MSD	Mean squared deviation [W^2 m^{-4}]
nRMSD	Normalized root mean squared deviation [%]
R_d	Diffuse transposition factor [dimensionless]
R^2	Coefficient of determination [unitless]
RMSD	Root mean squared deviation [W m^{-2}]
θ	Solar zenith angle [degrees]

Subscripts

bn	Beam normal
clear	Clear-sky
dh	Diffuse horizontal
gh	Global horizontal
gr	Ground reflection
gt	Global tilted
t	Tilted surface
toa	Top-of-atmosphere

Acronyms

BPV	Bifacial PV
BRL	Boland-Ridley-Lauret
BSRN	Baseline Surface Radiation Network
C	Temperate climate zone
CAMS	Copernicus Atmosphere Monitoring Service
CDF	Cumulative distribution function
GHG	Greenhouse gas emission
Cfb	Temperate oceanic microclimate zone
D	Cold climate zone
Dfc	Subarctic microclimate zone
E-W	East-West
MPV	Monofacial PV
PV	Photovoltaic
VBPV	Vertical BPV

Accurately estimating the global tilted irradiance (E_{gt}) on the plane of the array [10,11] is essential to evaluate the expected energy production and cost-effectiveness of various PV systems [12,13]. Due to the limited availability of solar irradiance data for tilted surfaces (i.e., availability of measurements for selected tilt angles and orientations), E_{gt} is commonly modelled from the global horizontal solar irradiance (E_{gh}). The modelling chain is typically initialized with E_{gh} and retrieved via direct measurement with ground pyranometers and satellite techniques or physical models (i.e., numerical reanalysis). Decomposition models enable separating E_{gh} into the beam normal (alternatively direct normal) irradiance (E_{bn}) and the diffuse horizontal irradiance (E_{dh}) based on a cluster of chosen predictors (e.g., solar angles, clearness index, air mass). Finally, the transposition models estimate E_{gt} for an unobstructed surface based on E_{bn}, E_{dh}, sun position, surface orientation, and ground albedo value.

However, this modelling chain is sensitive to errors from various sources. Firstly, decomposition models are often parametrized with datasets that cover only part of the globe [14,15]. Thus, the state-of-the-art "quasi-universal models" can be outperformed by "locally parametrized models", especially in microclimates that are underrepresented in the parametrization stage of the first models [16]. Secondly, the method used to estimate the diffuse irradiance from the sky dome during the transposition stage impacts the results' accuracy. Indeed, transposition models can model the light diffusion either by isotropic [17] or anisotropic [18,19] sky approach. The anisotropic sky approach is more accurate, but with low solar elevation angles, it is sensitive to errors due to high atmospheric thickness [20]. Therefore, low solar elevation angles (e.g., solar elevation lower than 5°) are often omitted in the parametrization [21,22], causing certain model chains to be unreliable under specific conditions (i.e., low solar elevation angles). With conventional PV installations at low- and mid-latitudes this omission is only a minor drawback since the energy production with low solar elevation is negligible. However, considering the combination of high-latitude locations and VBPV, a significant fraction of the total annual production occurs when the Sun is low above the horizon. This occurrence highlights the need for decomposition-transposition modelling chains developed and validated specifically using locally measured data.

1.1. Aims and structure of the study

This study aims to contribute to filling up the literature gap in solar irradiance modelling considering high-latitude locations and irradiation on eastwards and westwards vertically oriented PV surfaces. By reviewing the state-of-the-art decomposition [14,23] and transposition [24] models, 29 decomposition and 25 transposition models are chosen for detailed evaluation through model chains. All possible decomposition-transposition chains (725 chains) are used to calculate E_{gt} on vertical, East- and West-facing surfaces based on measured weather data and E_{gh} from Turku, Finland (60°N). The results are validated against measured E_{gt} with suitable statistical indicators. Finally, recommendations on how solar irradiance on VBPV setups should be modelled at high-latitude locations are provided.

The article is structured as follows: Section 2 presents the methodology, including the developed workflow, justification for the chosen decomposition and transposition models, the data quality control procedures, and statistical indicators. Section 3 presents a comprehensive comparison of the studied model chains, the visualizations of the key results, and the recommendations on how the irradiance on VBPV can be modelled. Finally, Section 4 concludes the article and suggests future developments.

2. Materials and methods

2.1. Workflow

The workflow followed in this study moves from the experimental monitoring of the E-W VBPV systems in Turku to the validation of multiple combinations of solar decomposition and transposition models, as well as to the identification of the best-performing solar model chain for each of the VBPV sides. Overall, the workflow is arranged into six stages (Fig. 1): (i) data acquisition, (ii) review of existing solar decomposition and transposition models, (iii) implementation of the models' library, (iv) initialization of the model chains to estimate solar irradiance on the front and rear of the VBPV, (v) experimental validation, and

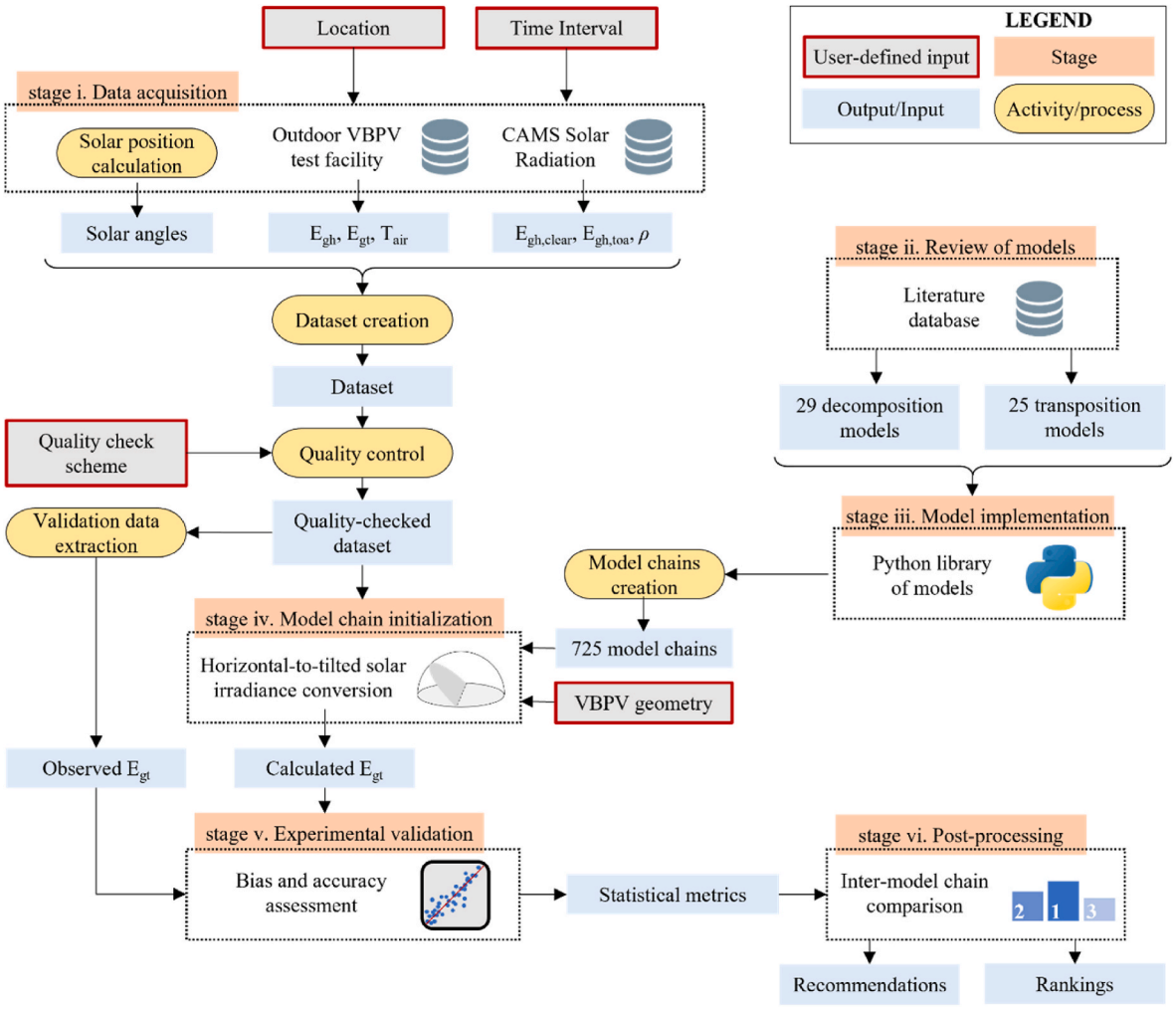

Fig. 1. Visualization of the workflow followed in this study.

(vi) inter-model chain comparison.

During *stage i. Data acquisition*, data is acquired either from the Copernicus Atmosphere Monitoring Service (CAMS) open-access database[1] [25–28] as well as from the database linked to the experimental facility in Turku. Solar irradiance measurements are collected from two vertically mounted pyranometers installed on the front and on the rear side of the E-W VBPV. The pyranometer type is Kipp & Zonen SMP10, Spectrally Flat Class A, measuring over a wavelength range from 285 nm to 2800 nm. Furthermore, a weather station equipped, among the others, with two horizontal second class pyranometers and a thermometer completes the data monitoring system in Turku. All data (e.g., ambient temperature and solar irradiance variables) are retrieved with a 1-min time resolution. A more detailed description of the dataset creation and the included variables is provided in the specific sub-section 2.4.

The literature research about solar decomposition and transposition models represents the core of *stage ii. Review of models*, review and validation studies either introducing new models or comparing the performance of the existing models are searched. In the context of decomposition models, the validation study by Gueymard and Ruiz-Arias [14] and the novel study by Yang [23] are considered the main references in selecting the decomposition models to investigate further. Solar decomposition models developed for hourly applications are hereby applied to 1-min analyses considering the issues related to cloud enhancement phenomena which have been highlighted by Gueymard and Ruiz-Arias [29]. Regarding the transposition models, the review from Yang [24] offers benchmark transposition models that can be combined with the previous decomposition models for being tested at high latitudes.

Stage ii. Model implementation focuses on implementing the models' library in *Python* programming language. Up to 29 decomposition and 25 transposition models are added to the library. Then, models are combined into multiple model chains: a decomposition model in the first part and a transposition model in the second part. Each model chain allows the decomposition of E_{gh} into E_{bn} and E_{dh}, and the transposing of these quantities into E_{gt}, according to the specific models' predictors (see Section 2.4). The outputs from the decomposition modelling (i.e., E_{bn} and E_{dh}) are the inputs of the transposition modelling. A more detailed description of the functioning of the model chain can be found in Manni et al. [30]. In total, 725 possible combinations are investigated to be applied on both the front and the rear sides of the VBPV. Regarding the taxonomy applied to the model chains, these are named according to the used decomposition and transposition model: the decomposition model name is separated from the name of the transposition model by the "/". For example, the model chain resulting from the combination of the Yang4 and the Steven1 models is named "Yang4/Steven1".

In *stage iv. Model chain initialization*: the 725 model chains are initialized with data retrieved during *stage i. Data acquisition* (e.g., E_{gh}, solar position, air mass, ambient temperature). Horizontal-to-vertical

[1] ads.atmosphere.copernicus.eu (Accessed on 07-07-2023).

irradiance conversion is performed for the front and rear sides of the E-W VBPV. Output quantities about E_{gt} are written into a new dataset in which the column headings report the names of the decomposition and transposition models analyzed in the calculation.

The experimental validation of the model chain outputs against measured E_{gt} values is performed in *stage v. Experimental validation*. The six statistical metrics described in sub-section 2.5 are calculated to provide a comprehensive overview of the model accuracy and overall performance by considering the model complexity (i.e., number of input parameters).

Finally, the *stage vi. Post-processing* consists of the analysis of the statistical metrics for inter-model chain comparison. The comparison is performed visually through the Taylor diagram and statistically with a score calculated for each model chain. In particular, the score is estimated as follows:

i. Model chains are ranked based on each chosen indicator separately.
ii. Based on the position occupied by the model chain on these rankings, a score is given to the top ten model chains (i.e., a score of 10 is assigned to the model chain in the 1st place, while a score of 1 is attributed to the model chain in the 10th place).
iii. The overall score of the model chain is ultimately calculated by summing the six specific scores (i.e., the scores according to each of the six rankings).

For example, suppose the model chain A occupies the 1st place in ranking one, the 4th place in ranking two, and it is absent from the best ten model chains in the other four rankings, two specific scores of 10 and 7 are assigned for the position in ranking one (1st place) and two (4th place), respectively. No score is given for the other rankings. Therefore, the final score for model chain A is 17.

As it is, the score permits the evaluation of how often and in which position a model chain occurs to be listed among the best ten model chains for the investigated statistical metrics by easing their comparison as well as the identification of the most effective modelling option for E-W VBPV at high latitudes.

2.2. Decomposition models' selection

The extensive validation performed by Gueymard and Ruiz-Arias [14] and the worldwide validation from Yang [23] have supported the selection of the decomposition models to exploit for solar irradiance separation analysis in Turku. Gueymard and Ruiz-Arias reviewed 140 decomposition models, most of which involved hourly datasets, while Yang focused on 1-min models developed later than 2016. Based on the normalized root mean squared deviation (nRMSD) values calculated by Gueymard and Ruiz-Arias [14], the best ten performing models per each climate zone present in the Nordics, such as temperate, cold, and polar climates [31], are shown in Table 1. Decomposition models that occur in any of the rankings are chosen to be tested in this study. Following this, Skartveit1 [32], Skartveit3 [33], Erbs [34], Perez1 [35], Perez2 [36], Perez3 [10], Muneer2 [37], Reindl2 [38], Reindl3 [38], Mondol1 [39], Mondol2 [40], Spencer [41], and DeMiguel [42] models are selected. A detailed description of the solving equations that are implemented in these models can be found in the respective referenced works.

Similarly, the models developed after 2016 and validated in Yang [23] are ranked according to the nRMSD calculated for C-zone, D-zone, and E-zone (top ten shown in Table 2). The Paulescu [43], Starke1 [44], Starke2 [44], Starke3 [16], Engerer2 [45], Engerer4 [46], Yang1 [47], Yang2 [47], Yang4 [48], Abreu [49], Every1 [50], and Boland-Ridley-Lauret (BRL) [51] models are added to the previous ones. A detailed description of the solving equations that are implemented in these models can be found in the respective referenced works. However, a few aspects concerning the model implementation in this work are worth highlighting. Regarding the Starke3 model, the set coefficients parametrized for the temperate (C) (Starke3C) and cold (D) (Starke3D) climate zones according to Köppen-Geiger classification [31], as well as for temperate oceanic (Cfb) (Starke3Cfb) and the subarctic (Dfc) (Starke3Dfc) microclimate zones are considered. Additionally, the Every2 model, which is listed in Table 2 but absent from the models investigated in this study, uses a set of coefficients determined for different climate zones similarly. However, when applied to cold climates, the Every2 model exploits the original coefficients from the BRL model; therefore, the BRL is here used instead. Finally, it is worth mentioning that the difference between nRMSD values in Table 1 is low, and it might be due to, among others, uncertainty in the experimental data or uncertainty propagation through the parameters of the model. While this approach may lead to potential inaccuracies in selecting the decomposition models to investigate, the reliability of the broader study remains.

The two groups of models are implemented in the model chains to estimate the solar irradiance on the two sides of the E-W VBPV with a 1-min time resolution. Indeed, certain hourly decomposition models may not be specifically designed to handle high-clearness index conditions, which include cloud enhancement events typically observed in 1-min outputs. However, with proper considerations, these models can still be utilized for sub-hourly analyses, as highlighted in [29].

Finally, decomposition models are here applied considering the following assumptions: (i) the atmosphere is modelled as a homogeneous medium in terms of temperature, pressure, and humidity over the area of interest; (ii) the atmospheric composition is standard for air density and composition of gases; (iii) the terrain is a flat surface without significant topographical variations; (iv) the high quality of input data is assured; and (v) the ground albedo is spatially uniform across the investigated surface.

Table 1
Calculated error statistics about E_{bn} for the high-latitude locations from supplementary material by Gueymard and Ruiz-Arias [14]. The best ten performing models for each climate zone in the Nordics and globally are listed, with statistics averaged over the selected sites.

C zone		D zone		E zone		Global[a]	
Model	nRMSD [%]	Model	nRMSD [%]	Model	nRMSD [%]	Model	nRMSD [%]
Skartveit1	12.70	Skartveit1	9.39	Spencer	12.70	Skartveit1	11.32
Perez2	13.16	Perez3	9.62	Muneer2	12.82	Mondol1	11.76
Skartveit3	13.26	Mondol1	9.77	Mondol2	12.87	Muneer2	11.76
Muneer2	13.35	Perez1	9.88	Mondol1	13.03	Perez3	11.80
Perez3	13.36	Reindl2	9.90	Skartveit1	13.05	Reindl2	12.00
Mondol1	13.44	Muneer2	9.95	Reindl3	13.23	Skartveit3	12.01
Reindl2	13.44	Skartveit3	10.12	Perez3	13.76	Mondol2	12.12
Mondol2	13.73	Perez2	10.13	Orgill	13.79	Perez1	12.35
Perez1	13.91	Orgill	10.20	Erbs	13.85	Orgill	12.40
Reindl3	14.15	DeMiguel	10.21	DeMiguel	13.85	DeMiguel	12.43

[a] Global amounts are estimated considering all the weather stations considered in the study.

Table 2
Calculated error statistics about E_{bn} for the high-latitude locations from supplementary material by Yang [23]. The best ten performing models for each climate zone in the Nordics and globally are listed, with statistics averaged over the selected sites.

C zone		D zone		E zone		Global[a]	
Model	nRMSD [%]	Model	nRMSD [%]	Model	nRMSD [%]	Model	nRMSD [%]
Yang4	19.44	Yang4	23.41	Yang4	28.33	Yang4	22.02
Starke3C	20.19	Starke1	24.05	Engerer2	29.68	Starke1	23.05
Starke1	20.44	Starke3D	24.18	Starke1	30.07	Engerer2	24.33
Engerer2	21.94	Engerer2	25.96	Paulescu	31.68	Starke3	24.75
Starke2	22.55	Paulescu	26.69	Engerer4	32.07	Paulescu	25.71
Paulescu	23.43	Starke2	26.89	Starke2	34.92	Starke2	25.83
Engerer4	25.21	Engerer4	28.93	Abreu	37.79	Engerer4	27.37
Abreu	27.02	Abreu	31.01	Every2	39.45	Abreu	29.93
Every1	31.15	Every2	33.57	Starke3E	40.42	Every2	33.45
Every2	31.56	Every1	36.65	Every1	42.05	Every1	34.48

[a] Global amounts are estimated considering all the weather stations considered in the study.

2.3. Transposition models

The benchmark models to estimate the solar irradiance on inclined surfaces investigated in Yang [24] are considered for being tested in Turku. The study reviews the most common physical and empirical transposition models. 25 transposition models are described by the equations for calculating the diffuse transposition factor (R_d). All the models investigated in Yang [24] are chosen to be integrated into the model chains implemented in this work: Liu [17], Bugler1 [52], Bugler 2 [53], Temps [54], Klucher [55], Steven1 [56], Steven2 [56], Steven3 [57], Steven4 [57], Hay1 [58], Hay2 [59], Willmott [60], Koronakis [61], Perez1 [62], Perez2 [63], Perez3 [64], Perez 4 [22], Skartveit [65], Gueymard [66], Muneer1 [67], Muneer2 [67], Reindl [68], Olmo [69], Tian [70], and Badescu [71]. A detailed description of the solving equations that are implemented in these models can be found in [24].

The diffuse transposition factor quantified by the transposition models is used to estimate the solar irradiation impinging on the two sides of the VBPV. In this regard, E_{gt} is considered as the sum of three contributions, namely the beam tilted irradiance (E_{bt}), the diffuse tilted irradiance (E_{dt}), and the ground reflections (E_{gr}). These are computed as:

$$E_{bt} = E_{bn} \cdot \cos aoi \tag{1}$$

$$E_{dt} = E_{dh} \cdot R_d \tag{2}$$

$$E_{gr} = \rho \cdot E_{gh} \cdot R_r \tag{3}$$

where *aoi* is the angle of incidence, ρ is the ground albedo, and the R_r factor is determined according to the isotropic assumption by Gueymard (4) [72].

$$R_r = \frac{1 - \cos \theta_t}{2} \tag{4}$$

where θ_t is the tilt angle of the surface.

2.4. Dataset implementation and quality control

A dataset is created to store input data required either to initialize the model chains (e.g., E_{gh}, solar zenith and azimuth angles, air mass, angle of incidence of sunrays) or to validate the outcomes (i.e., E_{gt}). Both radiometric and non-radiometric data from Turku are presented with a 1-min time-resolution from the July 4, 2019 to the October 20, 2020. Among the radiometric data, E_{gh}, as well as E_{gt} incident on the front (eastwards surface) and the rear (westwards surface) of the VBPV are measured with second class pyranometers in the experimental facility in Turku. It is worth reporting that the E_{gh} values are collected by two pyranometers so that the two E_{gh} time series can be compared to improve the data quality. In addition to ground observations (i.e., observations recorded at ground level), the CAMS is accessed to retrieve data about E_{gh} under clear-sky ($E_{gh,clear}$), E_{gh} at the top of the atmosphere ($E_{gh,toa}$), and ground albedo.

Regarding non-radiometric data, information about the solar position, geometry of the investigated surface, and atmosphere characteristics is determined through different functions of *pvlib* Python library. Apparent Solar Time (AST), as well as zenith and azimuth angles, are defined through the *ephemeris* and *location* function, respectively. Solar zenith (θ) and azimuth (α) angles together with surface tilt (θ_t) and azimuth (α_t) angles, are also used to quantify the angle of incidence (*aoi*) of the sunrays through the specific function (i.e., *irradiance. aoi* function from *pvlib*). In particular, the equation which is exploited by the *irradiance. aoi* function is the following one:

$$aoi = \cos^{-1}(\cos\theta_t \cdot \cos\theta + \sin\theta_t \cdot \sin\theta \cdot \cos(\alpha - \alpha_t)) \tag{5}$$

Furthermore, the air mass is quantified through the *atmosphere* function for each timestamp, while the weather station in Turku measured the ambient temperature.

To ensure the reliability of E_{gh} data, the observations are verified against both physically possible limits (6) and extremely rare minimum limits (7) during tests A and B, respectively. These are range tests (i.e., tests used to assess whether a set of data falls within a specific range of values) that were introduced by Long and Shi [73] and are currently applied within the Baseline Surface Radiation Network (BSRN).

$$-4\ W/m^2 < E_{gh} < 1.5 \cdot E_{bn,toa} \cdot \cos^{1.2}\theta + 100\ W/m^2 \tag{6}$$

$$-2\ W/m^2 < E_{gh} < 1.2 \cdot E_{bn,toa} \cdot \cos^{1.2}\theta + 50\ W/m^2 \tag{7}$$

where $E_{bn,toa}$ is the beam normal irradiation outside the atmosphere and θ is the zenith angle.

Furthermore, two additional tests are carried out to check ambient conditions and exclude any measurements affected by anomalies in the monitoring campaign (e.g., temporary shading of the sensor, inter-building reflection phenomena, sensor obstruction due to snow or dust). Firstly, during test C, the observations are compared to the upper possible limit for solar irradiation influenced by cloud enhancement effects (8). In this regard, the limit considered in this study is the one identified in [74] for the Nordics, and it is equal to 1.5 times $E_{gh,clear}$. Secondly, test D (9) is performed to verify that the relative deviation between the two E_{gh} observation time series ($E_{gh,1}$ and $E_{gh,2}$) is not due to sensor accuracy (i.e., the relative difference of E_{gh} values less than 5%) and take place in the presence of sky conditions that exclude the possible occurrence of cloud enhancement events (i.e., clearness index (k_t) equal or lower than 0.8 and clear-sky index for global horizontal irradiance (K_{CSI}) equal or lower than 0.95), as identified by Starke et al. [44].

$$E_{gh} \leq 1.5 \cdot E_{gh,clear} \tag{8}$$

$$\left|\frac{E_{gh,1} - E_{gh,2}}{E_{gh,1}}\right| \leq 0.05 \text{ if } K_{CSI} \leq 0.95 \text{ and } k_t \leq 0.8 \tag{9}$$

Finally, temporal filtering is performed by excluding the datapoints with solar zenith angles greater than 90° (i.e., night hours) from the dataset (test E).

The data quality control reduced the length of the datasets from circa 684,060 datapoints to circa 321,610 datapoints. An overview of the test results is reported in Table 3.

2.5. Statistical metrics

The statistical metrics used to identify the most adequate solar irradiance model chain for E-W VBPV applications at high latitudes are chosen from the comprehensive overview of performance metrics provided by Gueymard [75]. Indicators of the dispersion of individual points (class A in [75]), such as mean squared deviation (MSD), the root mean squared deviation (RMSD), the coefficient of determination (R^2), the mean biased deviation (MBD), the mean absolute deviation (MAD), and the mean absolute percent deviation (MAPD) are calculated as it follows:

$$MSD = \frac{\sum_{i=1}^{N}(o_i - m_i)^2}{N} \tag{10}$$

$$RMSD = \sqrt{\frac{\sum_{i=1}^{N}(o_i - m_i)^2}{N}} \tag{11}$$

$$R^2 = \left[\frac{\sum_{i=1}^{N}(m_i - \overline{m})\cdot(o_i - \overline{o})}{\sum_{i=1}^{N}(m_i - \overline{m})^2\cdot(o_i - \overline{o})^2}\right]^2 \tag{12}$$

$$MBD = \frac{\sum_{i=1}^{N}(o_i - m_i)}{N} \tag{13}$$

$$MAD = \frac{\sum_{i=1}^{N}|o_i - m_i|}{N} \tag{14}$$

$$MAPD = \frac{100}{\overline{o}}\cdot\frac{\sum_{i=1}^{N}|o_i - m_i|}{N} \tag{15}$$

where o_i and m_i are, respectively, the i-th observed and modelled values, N is the total number of datapoints, and $\overline{o}$ and $\overline{m}$ are the mean values of observations and modelled quantities.

These metrics are widely used in validation studies and enable assessing different aspects of the model chain performance. In this regard, MSD and RMSD have sensitivity to errors by penalizing the larger ones (although with a different magnitude), the R^2 provides information on how well the model fits the reference data, the MBD allows identification of any existent directional bias (over- or under-estimation), and MAD and MAPD provide insight into the average magnitude of the errors. Their value would be 0 (or 1 in the case of R^2) for a perfect model. It is worth noting that since the model chains are validated with the same benchmark data from the same case study location, normalizing the statistical metrics is deemed unnecessary as it fails to contribute any additional information to the results. Nonetheless, the average value of E_{gt} observations used to validate the model chain outcomes is provided here to compare results from different research works (i.e., using normalized statistic metrics). In particular, the average E_{gt} value equals 201.10 W m^{-2} for the East-facing surface and 139.72 W m^{-2} for the West-facing surface.

Table 3
Number of datapoints that are filtered out by each test.

Excluded datapoints	
Test A	1,252
Test B	9,474
Test C	14,741
Test D	22,596
Test E	324,847

Among the class C indicators (i.e., indicators of distribution similitude) presented in [75], the Kolmogorov–Smirnov test Integral (KSI) developed by Espinar et al. [76] is considered to assess the similarity or dissimilarity between the cumulative distribution functions (CDFs) of modelled data and a reference dataset, identifying eventual systematic biases because of its advantage of being nonparametric and valid for any CDF. KSI is calculated as in (16):

$$KSI = \int_{x_{min}}^{x_{max}} D_n dx \tag{16}$$

where D_n is the absolute difference between the two normalized distributions within irradiance interval n.

Similarly, the OVER statistic from Espinar et al. [76], based on KSI, is also added. The OVER accounts for the differences between two CDFs when they exceed a critical limit (17).

$$OVER = \int_{x_0}^{x_1} Max(D_n - D_c, 0)dx \tag{17}$$

where the critical value, Dc, is a statistical characteristic of the reference distribution, defined as a function of its number of points, N.

The use of KSI and OVER brings a different kind of information than the more conventional indicators of class A and can also be more discriminant [75]. Therefore, the Combined Performance Index (CPI) (18) introduced in [77] is considered in this study to combine conventional information about dispersion and bias (through RMSD) with information about distribution likeness (through KSI and OVER) while maintaining a high degree of discrimination between different models. The same Gueymard [77] argued that, if a single statistical indicator had to be selected to compare the performance of models powerfully, the best choice would be CPI. The measuring unit of the CPI is W m^{-2}.

$$CPI = (KSI + OVER + 2\cdot RMSD)/4 \tag{18}$$

Finally, while it was not listed among the statistical metrics in [75], the Bayesian Information Criterion (BIC) [78] and the Akaike Information Criterion (AIC) are calculated.

$$BIC = -2\cdot\log\frac{\sum_{i=1}^{N}(o_i - m_i)^2}{N} + P\cdot\log N \tag{19}$$

$$AIC = -2\cdot\log\frac{\sum_{i=1}^{N}(o_i - m_i)^2}{N} + 2\cdot P \tag{20}$$

Both the BIC and AIC are particularly relevant in this study as well as in similar ones (i.e., selecting the best performing model) since they are the only statistical metrics among the listed ones that can evaluate the complexity of the modelling chain (i.e., the number of the input parameters, P) besides the quality of fit to the data. The BIC and AIC penalize those model chains that require too many input parameters, although with a different magnitude. A low BIC value, as well as a low AIC value, corresponds to a good trade-off between model simplicity and goodness of fit, which is important in solar irradiance modelling. Since the length of the datasets influences the calculation, there is no upper limit for BIC values, in theory.

3. Results and discussion

3.1. Model chain validation

Table 4 and Table 5 report, respectively, the top ten ranked model chains for the East-facing and West-facing sides of the VBPV, according to the chosen statistical indicators.

A detailed examination is reserved for model with 60% of the highest score (i.e., top five ranked model chains). According to their position in each of the nine rankings reported in Table 4 for the East-facing sides of

Table 4
Top ten ranked model chains for the East-facing side of the VBPV for each statistical indicator.

Models	MAD [W m^{-2}]	Models	MAPD [%]	Models	MBD [W m^{-2}]	Models	MSD [W^2 m^{-4}]	Models	RMSD [W m^{-2}]
Erbs/Steven4	68.27	Erbs/Steven4	32.89	Starke2Bra/Muneer2	−1.08	Erbs/Steven1	12,419	Erbs/Steven1	111.44
Paulescu/Steven4	70.22	Perez3/Steven4	33.87	Starke2Bra/Badescu	5.47	Perez3/Steven1	12,478	Perez3/Steven1	111.70
Perez3/Steven4	70.31	Erbs/Steven1	33.88	Starke2Bra/Temps	6.24	Erbs/Steven2	12,723	Erbs/Steven2	112.80
Erbs/Steven1	70.33	Erbs/Steven2	34.10	Starke2Aus/Temps	−7.01	Perez1/Steven1	12,741	Perez1/Steven1	112.88
Muneer2/Steven4	70.60	Perez1/Steven4	34.16	Starke2Aus/Badescu	−9.07	Perez3/Steven2	12,764	Perez3/Steven2	112.98
Demiguel/Steven4	70.72	Perez2/Steven4	34.44	Starke2Aus/Koronakis	9.53	Perez2/Steven1	12,771	Perez2/Steven1	113.01
Reindl3/Steven4	70.76	Perez3/Steven1	34.69	Starke3Dfc/Temps	11.19	Perez1/Steven2	13,061	Perez1/Steven2	114.28
Orgill/Steven4	70.78	Paulescu/Steven4	34.92	Starke3Dfc/Badescu	11.38	Perez2/Steven2	13,091	Perez2/Steven2	114.41
Erbs/Steven2	70.79	Perez1/Steven1	34.93	Starke3Dfc/Muneer2	11.79	Yang2/Steven1	13,289	Yang2/Steven1	115.28
Mondol1/Steven4	70.83	Perez3/Steven2	34.99	Starke2Aus/Willmott	12.70	Paulescu/Steven1	13,403	Paulescu/Steven1	115.77

Models	R^2 [-]	Models	CPI [W m^{-2}]	Models	AIC [W m^{-2}]	Models	BIC [W m^{-2}]
Erbs/Steven1	0.775	Erbs/Steven1	79.54	Yang2/Bugler1	0.02	Abreu/Steven3	3.96
Perez3/Steven1	0.774	Erbs/Steven2	80.78	Yang1/Klucher	0.03	Abreu/Liu	4.09
Erbs/Steven2	0.770	Reindl3/Steven1	81.04	Yang1/Bugler1	−0.04	Abreu/Tian	4.09
Perez1/Steven1	0.770	Perez3/Steven1	81.29	Yang2/Klucher	0.06	Abreu/Koronakis	4.25
Perez2/Steven1	0.769	Demiguel/Steven1	81.63	Perez2/Reindl	0.07	Abreu/Badescu	4.28
Perez3/Steven2	0.769	Orgill/Steven1	81.73	Perez1/Reindl	0.10	Mondol2/Steven3	4.28
Perez1/Steven2	0.764	Paulescu/Steven1	81.89	BRL/Reindl	−0.10	Muneer2/Steven3	4.29
Perez2/Steven2	0.763	Perez1/Steven1	81.92	Every/Reindl	−0.12	Mondol1/Steven3	4.36
Yang2/Steven1	0.751	Perez3/Steven2	82.16	Perez1/Gueymard	−0.12	Orgill/Steven3	4.37
Perez3/Olmo 1	0.751	Reindl3/Steven2	82.25	Starke2Bra/Reindl	−0.14	Demiguel/Steven3	4.39

Table 5
Top ten ranked model chains for the West-facing side of the VBPV for each statistical indicator.

Models	MAD [W m^{-2}]	Models	MAPD [%]	Models	MBD [W m^{-2}]	Models	MSD [W^2 m^{-4}]	Models	RMSD [W m^{-2}]
Yang2/Muneer1	53.51	Yang2/Muneer1	38.30	Starke2Aus/Hay1	−2.91	Yang2/Hay1	8,486	Yang2/Hay1	92.12
Yang1/Muneer1	55.68	Perez2/Muneer1	39.57	Starke2Aus/Hay2	−3.71	Yang2/Hay2	8,532	Yang2/Hay2	92.37
Perez2/Muneer1	56.68	Yang1/Muneer1	39.85	Starke2Aus/Muneer1	−5.60	Perez2/Hay1	8,777	Perez2/Hay1	93.69
Yang2/Hay1	57.40	Yang2/Hay1	41.05	Starke2Aus/Steven3	−19.52	Perez2/Hay2	8,834	Perez2/Hay2	93.99
Yang2/Hay2	57.59	Yang2/Hay2	41.18	Starke2Bra/Muneer1	−20.82	Yang2/Muneer1	8,877	Yang2/Muneer1	94.22
Yang4/Muneer1	57.87	Perez1/Muneer1	41.42	Starke2Bra/Hay1	−20.82	Starke21C/Hay1	8,926	Starke3C/Hay1	94.48
Yang1/Hay1	58.85	Yang4/Muneer1	41.42	Starke2Bra/Hay2	−21.47	Yang1/Hay1	8,939	Yang1/Hay1	94.55
Starke3C/Muneer1	59.04	Perez3/Muneer1	42.08	Yang2/Muneer1	−28.47	Starke3C/Hay2	8,989	Starke3C/Hay2	94.81
Yang1/Hay2	59.07	Yang1/Hay1	42.09	Starke3Dfc/Muneer1	−28.50	Yang1/Hay2	8,993	Yang1/Hay2	94.83
Engerer2/Muneer1	59.21	Starke3C/Muneer1	42.22	Abreu/Muneer1	−28.87	Abreu/Hay1	9,146	Abreu/Hay1	95.63

Models	R^2 [-]	Models	CPI [W m^{-2}]	Models	AIC [W m^{-2}]	Models	BIC [W m^{-2}]
Perez2/Hay1	0.742	Yang2/Muneer1	62.87	Starke2Aus/Reindl	0.03	Reindl3/Badescu	4.37
Yang2/Hay1	0.741	Yang2/Hay1	64.14	Starke3Dfc/Klucher	0.05	Orgill/Badescu	4.44
Perez2/Hay2	0.740	Yang2/Hay2	64.38	Starke3D/Klucher	0.06	Demiguel/Badescu	4.44
Yang2/Hay2	0.740	Abreu/Muneer1	65.34	Starke2Bra/Reindl	−0.09	Mondol2/Badescu	4.47
Perez2/Muneer1	0.730	Yang4/Muneer1	65.68	Engerer2/Skartveit	0.09	Muneer2/Badescu	4.53
Yang2/Muneer1	0.729	Starke3C/Muneer1	66.02	Engerer3/Skartveit	0.09	Reindl3/Koronakis	4.56
Starke21C/Hay1	0.728	Yang1/Hay1	66.02	Perez2/Steven4	−0.09	Mondol1/Badescu	4.62
Yang1/Hay1	0.728	Yang1/Muneer1	66.26	BRL/Gueymard	−0.10	Orgill/Koronakis	4.64
Starke3C/Hay2	0.726	Yang1/Hay2	66.33	Starke2Bra/Steven4	0.11	Paulescu/Badescu	4.64
Yang1/Hay2	0.726	Starke3Cfb/Muneer1	66.92	Perez1/Steven4	−0.15	Demiguel/Koronakis	4.65

the VBPV, the model chains Erbs/Steven1 (score 55 based on method presented in sub-section 2.1), Erbs/Steven2 (42), Perez3/Steven1 (38), Perez1/Steven1 (26), and Erbs/Steven4 (20) are the ones characterized by the highest scores.

An overview of the statistical metrics calculated for these model chains is reported in Table 6, while the visual comparison of observations and modelled values is provided in Fig. 2. The best five model chains are characterized by MAD and RMSD values ranging from 68.27 W m^{-2} (Erbs/Steven4) to 72.60 W m^{-2} (Perez1/Steven1) and from 111.44 W m^{-2} (Erbs/Steven1) to 117.80 W m^{-2} (Erbs/Steven4), respectively. Although the modelled values well fit the observations (i.e., R^2 values are circa 0.770) and the two series show a good agreement (i.e., Pearson correlation coefficient in the supplementary material is higher than 0.90), the model chains showed the tendency to overestimate E_{gt} on the East side of the VBPV (i.e., MBD varies from 34.85 W m^{-2} to 53.88 W m^{-2}).

An insight into the overall performance of the model chains and goodness of fit weighted for model complexity is provided through CPI, BIC, and AIC. The five model chains show the lowest values for CPI, which ranges between 79.54 W m^{-2} (Erbs/Steven1) and 85.19 W m^{-2} (Erbs/Steven4) (average and highest values are 111.06 W m^{-2} and 159.18 W m^{-2}), while the BIC values vary between 42.58 W m^{-2} and 79.30 W m^{-2} (average and highest values are 73.55 W m^{-2} and 140.51 W m^{-2}). Finally, AIC varies from −3.08 W m^{-2} (Erbs/Steven4) to −8.90 W m^{-2} (Erbs/Steven2) (average and highest values are −4.89 W m^{-2} and 6.56 W m^{-2}). The average and the highest values are estimated considering every model chain.

When it comes to the West-facing sides of the VBPV, the model chains Yang2/Hay1 (52), Yang2/Muneer1 (50), Yang2/Hay2 (45), Perez2/Hay1 (26), and Perez2/Muneer1 (23) show the highest scores, according to their position in each of the six rankings reported in Table 5.

Table 6
Statistical indicators for the best five model chains for the East side together with minimum, maximum, and average values of the used metrics.

	MAD [W m^{-2}]	MAPD [%]	MBD [W m^{-2}]	MSD [W^2 m^{-4}]	RMSD [W m^{-2}]	R^2 [-]	CPI [W m^{-2}]	AIC [W m^{-2}]	BIC [W m^{-2}]
Erbs/Steven1	70.33	33.88	39.72	12,419	111.44	0.775	79.54	−8.85	42.63
Erbs/Steven2	70.79	34.10	40.95	12,723	112.80	0.770	80.78	−8.90	42.58
Perez3/Steven1	72.02	34.69	34.85	12,478	111.70	0.774	81.29	−8.86	42.62
Perez1/Steven1	72.60	34.93	35.16	12,741	112.88	0.770	81.92	−4.91	67.16
Erbs/Steven4	68.27	32.89	53.88	13,876	117.80	0.749	85.19	−3.08	79.30
Minimum	68.27	32.89	−23.43	12,419	111.44	−0.399	79.54	−16.78	3.96
Average	92.29	45.30	54.22	23,670	152.47	0.563	111.06	−4.89	73.55
Maximum	175.38	87.14	95.44	74,726	273.36	0.775	159.18	6.56	140.51

The statistical metrics that are estimated for these model chains are provided in Table 7. In addition, the visual comparison of observations and modelled values is outlined in Fig. 3. The MAD and RMSD of the best five model chains range from 53.51 W m^{-2} (Yang2/Muneer1) to 60.87 W m^{-2} (Perez2/Hay1) and from 92.12 W m^{-2} (Yang2/Hay1) to 95.88 W m^{-2} (Perez2/Muneer1), respectively. The R^2 values (circa 0.740) suggest that modelled values well fit observations. However, the model chains tend to under-estimate E_{gt} on the West side of the VBPV since the MBD varies from −28.47 W m^{-2} (Yang2/Muneer1) to −48.95 W m^{-2} (Perez2/Hay1).

Moreover, the five model chains show the lowest values for the CPI metric, which ranges between 62.87 W m^{-2} (Yang2/Muneer1) and 71.35 W m^{-2} (Perez2/Hay1) (average and highest values are 113.00 W m^{-2} and 183.95 W m^{-2}), while the BIC values are circa 100–120 W m^{-2} (average and highest values are 73.83 W m^{-2} and 142.62 W m^{-2}). Finally, AIC varies from −2.16 W m^{-2} (Perez2/Hay1) to 7.82 W m^{-2} (Yang2/Muneer1) (average and highest values are −4.61 W m^{-2} and 7.82 W m^{-2}).

3.2. Taylor diagrams

Additional information about the model's performance is reported in this section. Pearson correlation coefficients are estimated for the model chains and represented in the Taylor diagrams (Fig. 4) along with the standard deviation, MBD, and RMSD. The visual comparison of the statistical metrics calculated for each model chain permits a better understanding of differences in modelling performance among the investigated model chains.

3.3. Influences of surface orientations on model chain performance

The investigated model chains perform differently depending on the surface orientation. Model chains exploited to estimate E_{gt} impinging on the East-facing side of the VBPV are generally characterized by lower accuracy than model chains applied to the quantification of E_{gt} on the West-facing side (Fig. 5). In particular, the investigated model chains always over-estimate E_{gt} on the eastward-oriented surface, while under-estimating E_{gt} on the westward-oriented surface of the solar module.

The analysis of quartiles (i.e., the boxes plotted inside the violins in Fig. 5) permits a better understanding of the magnitude of this variation in terms of modelling performance.

For example, the first and the third quartiles associated with the RMSD series are equal to 138.49 W m^{-2} and 165.64 W m^{-2} (median is 153.08 W m^{-2}) for the East surface, and to 128.85 W m^{-2} and 157.10 W m^{-2} (median is 144.69 W m^{-2}) for the West surface. Similarly, the first and the third quartiles associated with the MBD series are 40.78 W m^{-2} and 65.31 W m^{-2} (median is 55.86 W m^{-2}) for the East-facing surface, and −92.13 W m^{-2} and -70.42 W m^{-2} (median is −83.69 W m^{-2}) for the West-facing surface. Moreover, it is worth highlighting that moving from the East to the West side of the VBPV can cause a worsening of CPI

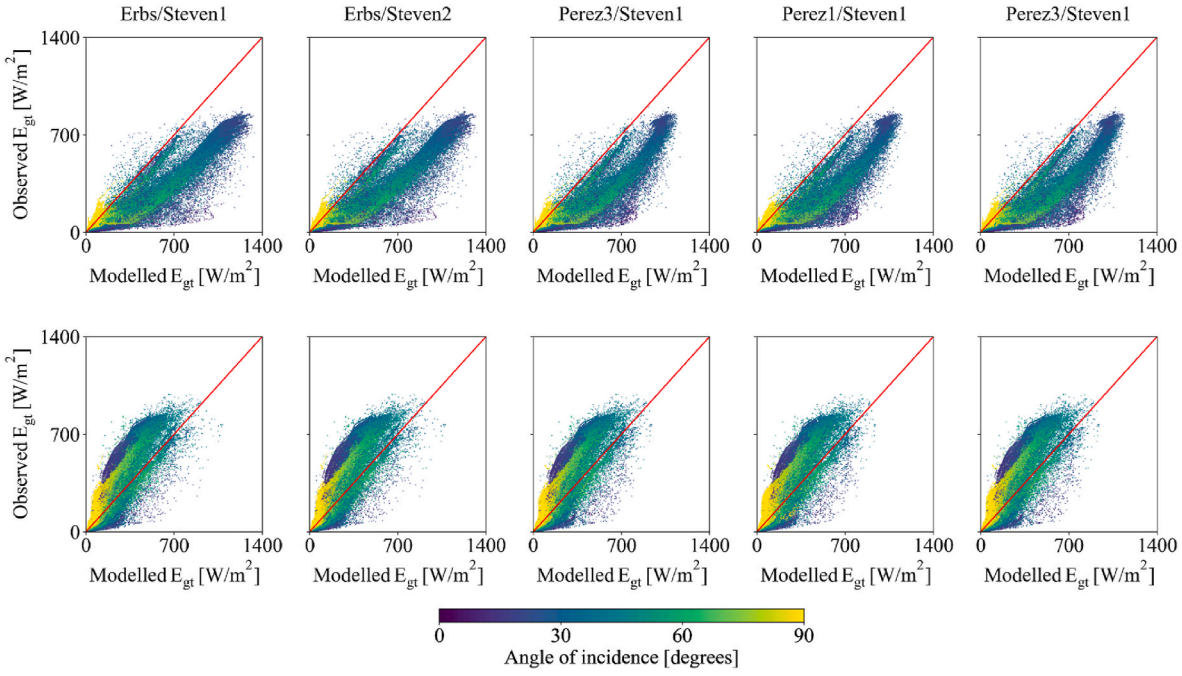

Fig. 2. Scatter plots of the best five model chains for the East side: observed E_{gt} is plotted against the modelled E_{gt} for the West- (top) and the East-facing surface (bottom). Datapoints are colored based on the respective angle of incidence value.

Table 7
Statistical indicators for the best five model chains for the West side together with minimum, maximum, and average values of the used metrics.

	MAD [W m^{-2}]	MAPD [%]	MBD [W m^{-2}]	MSD [W^2 m^{-4}]	RMSD [W m^{-2}]	R^2 [-]	CPI [W m^{-2}]	AIC [W m^{-2}]	BIC [W m^{-2}]
Yang2/Hay1	57.40	41.05	−32.05	8,486	92.12	0.741	64.14	1.91	105.59
Yang2/Muneer1	53.51	38.30	−28.47	8,877	94.22	0.729	62.87	7.82	142.62
Yang2/Hay2	57.59	41.18	−32.45	8,532	92.37	0.740	64.38	1.90	105.58
Perez2/Hay1	60.87	42.47	−48.95	8,777	93.69	0.742	71.35	−2.16	80.19
Perez2/Muneer1	56.68	39.57	−45.01	9,192	95.88	0.730	69.83	3.75	116.99
Minimum	53.51	38.30	−126.06	8,486	92.12	−0.516	62.87	−16.36	4.37
Average	93.09	65.96	−79.66	20,898	142.69	0.372	113.00	−4.61	73.83
Maximum	140.96	100.80	−2.91	49,742	223.03	0.742	183.95	7.82	142.62

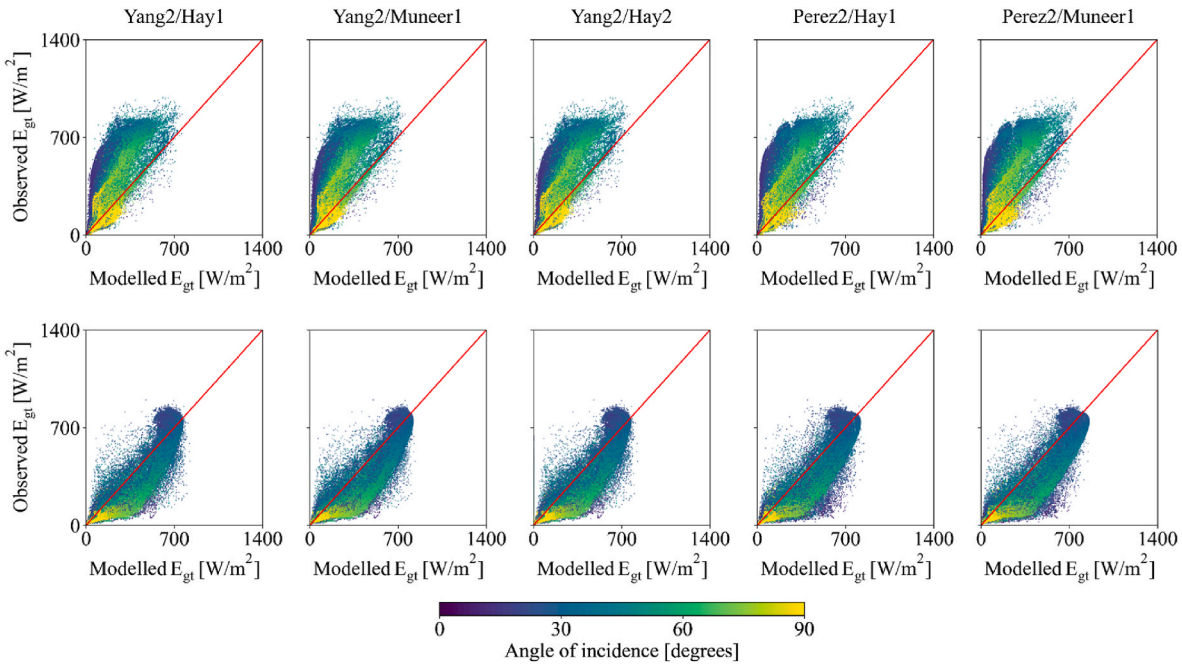

Fig. 3. Scatter plots of the best five model chains for the West side: observed E_{gt} is plotted against the modelled E_{gt} for the West- (top) and the East-facing surface (bottom). Datapoints are colored based on the respective angle of incidence value.

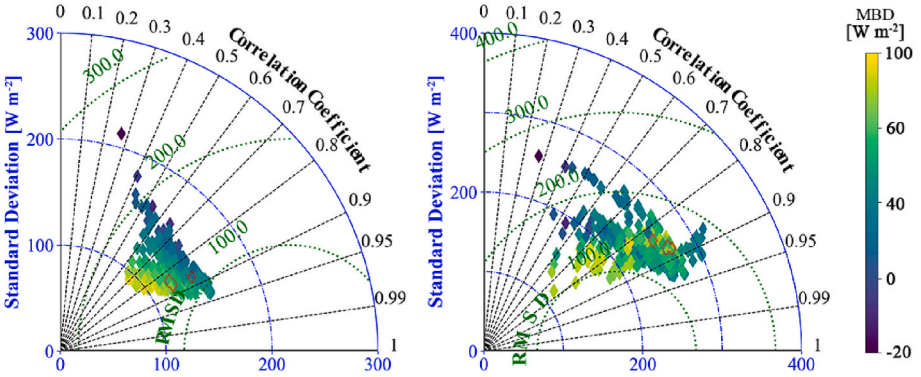

Fig. 4. Taylor diagrams for the East (right) and West (left) sides of the VBPV. Each mark corresponds to a model chain and is colored according to the corresponding MBD. Marks with red edges highlight the positions in the graph of the top five model chains for each side. Note that the five marks with red edges can overlay in the Taylor diagram since they have similar statistical metrics.

from 101.59 W m^{-2} to 100.76 W m^{-2} (first quartile) as well as from 120.81 W m^{-2} to 126.31 W m^{-2} (third quartile). However, a complete description of the quartiles calculated for each statistical indicator is provided in Fig. 5 and in supplementary materials.

A closer look at the specific performance of the top-ranked model chain for the two VBPV sides (i.e., Erbs/Steven1 for the East and Yang2/Hay1 for the West) permits to investigate how the statistical metrics change (Table 8). While there is a minimum variation in the Yang2/Hay1 when comparing the outcomes from the analysis of the two sides of BIPV, the statistical metrics calculated for the Erbs/Steven1 model chain turn out to be significantly worsened. RMSD, MAD, and CPI that are estimated for the East-facing side are almost doubled when it comes to the West. On the contrary, the R^2 coefficient is more than halved, resulting in a lower accuracy. A potential reason for such a behavior can

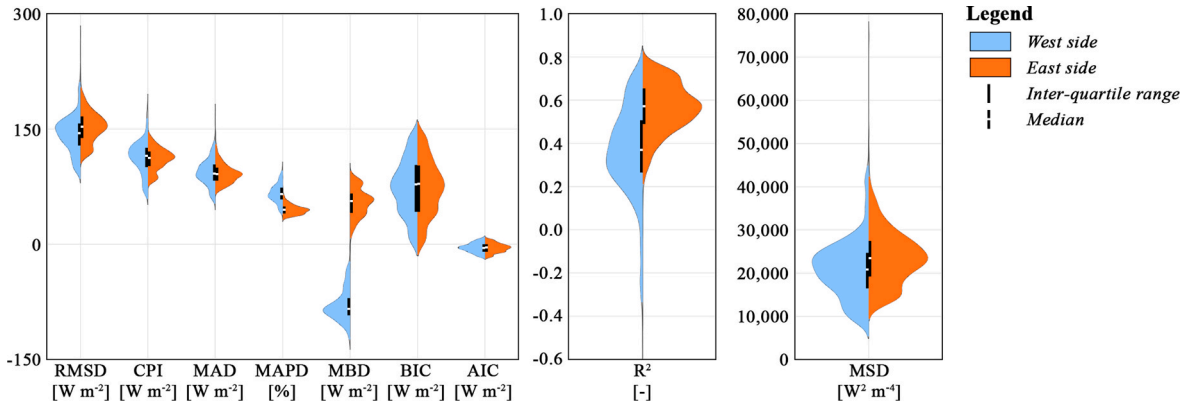

Fig. 5. Frequency distributions of the statistical metrics calculated for the model chains applied to the West (light blue) and on the East side (orange). The inter-quartile range (i.e., range between the first and third quartile) and the median are shown inside the violins.

be identified by assessing the scatterplots in Figs. 2 and 3. In particular, the worsening of the model chain performance can be related to the lower capability of estimating solar irradiance with low angles of incidence (i.e., close to the surface normal) when it comes to the West VBPV side.

3.4. Recommendations on horizontal-to-vertical irradiance conversion

This study demonstrates that it is hard to identify a single model chain that can perform the best, regardless of the surface orientation, at high latitudes. Model chains optimally operating for the East side of the panel achieve a different level of accuracy when modelling solar irradiance impinging on the West side. Nonetheless, some recommendations can be identified to help select the model chain for estimating the solar energy potential of E-W VBPV at high latitudes.

The experimental validation of the model chains with solar irradiation data from the East side of the VBPV shows that the Erbs model, together with transposition models from the Steven family of models, should be recommended for horizontal-to-vertical solar irradiance conversion at high latitudes. Therefore, in this case, local models (i.e., models parametrized with climate-specific datasets) are outperformed by models presented as "quasi-universal". Also, the Perez model family combined with either Steven1 or Steven2 model can be considered for being combined into a model chain with similar performance levels despite a higher number of input parameters (7 instead of 5) when considering the Perez1 model.

When it comes to the experimental validation, which is performed for the West-facing surface of the VBPV, the results have demonstrated that the transposition model developed from Hay as well as from Muneer can be considered the most adequate to transpose E_{dh} and E_{dn} into E_{gt}, being this present in three model chains in the top five shortlist. In this case, the decomposition models from the Yang and Perez model families are found to be the most effective when combined with the Hay1 into the model chain for horizontal-to-vertical solar irradiance conversion.

In conclusion, the following recommendations can be outlined for horizontal-to-vertical solar irradiance conversion at high latitudes:

- Using two different model chains for the front and rear sides of the VBPV can increase the results' accuracy.
- Models from the families of Yang and Perez should be preferred for the solar decomposition stage when assessing the West side of the VBPV.
- Erbs models and Perez family of models should be preferred for the solar decomposition stage when assessing the East side of the VBPV.
- Hay and Steven families of transposition models should be preferred for the West and East application, respectively.

3.5. Further discussion

Findings from previous studies have been confirmed by these outcomes. The Engerer2 decomposition model is excluded from the best model chains since it loses accuracy in locations characterized by high albedo. Other popular decomposition models, such as DeMiguel, Maxwell, Orgill, Reindl2, and Skarveit2, behave similarly [14]. Although Erbs is listed along with these low-efficient models in [14], it is utilized in the best performing model chain for the East side of the BVPV. On the contrary, the Perez model family is confirmed to be a good option. Among the ten recent decomposition models (i.e., developed after 2016) validated by Yang, only the Yang2 is present in the best-performing model chains. In addition, both the Yang4 and the

Table 8
Changes in the statistical metrics of the top-ranked model chains for the two VBPV sides, Erbs/Steven1 (East-facing side) and Yang2/Hay1 (West-facing side).

Erbs/Steven1									
	MAD [W m^{-2}]	MAPD [%]	MBD [W m^{-2}]	MSD [W m^{-2}]	RMSD [W m^{-2}]	R^2 [-]	CPI [W m^{-2}]	AIC [W m^{-2}]	BIC [W m^{-2}]
East	70.33	33.88	39.72	12,419	111.44	0.775	79.54	−8.85	42.63
West	107.60	75.21	−105.04	29,543	171.88	0.131	139.81	−10.59	40.90
Variation	**53 %**	**122 %**	**−364 %**	**138 %**	**54 %**	**−83 %**	**76 %**	**20 %**	**−4 %**
Yang2/Hay1									
	MAD [W m^{-2}]	**MAPD [%]**	**MBD [W m^{-2}]**	**MSD [W m^{-2}]**	**RMSD [W m^{-2}]**	**R^2 [-]**	**CPI [W m^{-2}]**	**AIC [W m^{-2}]**	**BIC [W m^{-2}]**
East	89.07	44.26	73.36	24,159	155.43	0.548	113.68	−0.18	103.50
West	57.40	41.05	−32.05	8,486	92.12	0.741	64.14	1.91	105.59
Variation	**−36 %**	**−7 %**	**−144 %**	**−65 %**	**−41 %**	**35 %**	**−44 %**	**−1132 %**	**2 %**

Engerer2, which are claimed to be the best quasi-universal decomposition models, are not present in the best-performing model chains at high latitudes.

The conclusive remarks from Yang's study [24] highlighted that the Perez, Muneer, Hay, and Gueymard families of models can provide the most accurate results. The experimental validation of model chains for horizontal-to-vertical solar irradiance conversion which is here presented partially confirmed these findings. In particular, the Hay and Muneer families of models are found to perform optimally when applied to the estimation of E_{gt} on the West side of the VBPV, but they are outperformed by the Steven family of models (not recommended in [24]) when assessing the East-facing side of the panel.

Based on the findings of the study, if we had selected the decomposition and transposition models to be applied at high latitudes according to the worldwide validation and review articles referenced in this work [14,23,24], the most effective option would have hardly been used, particularly for the solar analysis on the East VBPV side.

3.6. Limitations of the study

The study presents some limitations. Firstly, the ground albedo values that are exploited to estimate the ground reflections when calculating the diffuse tilted irradiance are retrieved from satellite observations and not measured in the experimental field. These values are always lower than 0.35, which is a conservative assumption regarding the winter months with snow and ice covering the ground surface. In fact, albedo values for snow are highly variable, ranging from as high as 0.9 for freshly fallen snow, about 0.4 for melting snow, and as low as 0.2 for dirty snow [79]. However, this limitation equally impacts every investigated model chain without affecting the results of the comparative analysis.

Secondly, no quality filter is applied to data used for validation (E_{gt} on the front and rear of the VBPV) but only to the model chain's input (E_{gh} at the site). This is due to the lack of shared protocols for quality testing of E_{gt} data. Possible tests have been proposed in previous studies [80,81], but their application is debated since they need to be calibrated for the specific location and orientation of the sensors. The absence of quality tests can result in a lower data quality, leading to biased statistical metrics associated with the investigated model chains. Again, the same datasets are used for every model chain, thus not affecting the conclusion.

4. Conclusion and further developments

Model chains for horizontal-to-vertical solar irradiance conversion to use in E-W VBPV simulation at high latitudes are investigated. Experimental validation is performed with 1-min data about E_{gt} on the front and rear of the solar modules collected in Turku. A total of 29 decomposition models from Gueymard and Ruiz-Arias [14] and Yang [23] are combined with 25 transposition models [24] into 725 model chains.

The main findings of this study can be summarized in the following bullets:

- Accuracy and bias of the model chains are different for the East and West sides of the VBPV.
- Model chain Erbs/Steven1 is the top-ranked one (with scores of 55 out of 90) when assessing the East side of the VBPV.
- Model chain Yang2/Hay1 is the top-ranked one (with a score of 52 out of 90) when assessing the West side of the VBPV.
- The quasi-universal decomposition models Engerer2 and Yang4 are absent from the shortlisted model chains.

Therefore, to enhance the accuracy of the results from solar analysis, there is a need for a metamodel-based approach that can apply different model chains according to a parameter, such as the angle of incidence or the geometry of the investigated surface. Regarding the identification of the best model chain for a specific surface orientation (i.e., the ranking process from *stage iv. Post-processing*), it is worth highlighting that the outcomes strongly depend on both the type and number of the chosen statistical indicators. For example, adding or removing a statistical indicator might alter the model chain's score and its position in the ranking. This risk has been mitigated in this research study by calculating a wide range of statistical indicators representative of different aspects of the model chains. Nonetheless, a sensitive analysis should be performed in the future about the influences of the statistical indicators' selection on identifying the best model chain.

Other future research developments concern exploring how uncertainty propagates through the model's parameters and validating of the model chains for applications beyond E-W VBPV, considering locations other than Turku. Another room for advancement lies in implementing a metamodel-based approach, promising more accurate estimations of E_{gt}. Furthermore, a comprehensive investigation into the causes of errors, particularly those affecting the model's performance on West-facing versus East-facing vertical surfaces, presents an area for potential inquiry.

CRediT authorship contribution statement

Mattia Manni: Conceptualization, Methodology, Software, Validation, Formal analysis, Investigation, Data curation, Writing – original draft, Writing – review & editing, Visualization. **Sami Jouttijärvi:** Formal analysis, Writing – original draft, Writing – review & editing. **Samuli Ranta:** Resources, Data curation. **Kati Miettunen:** Writing – review & editing, Funding acquisition. **Gabriele Lobaccaro:** Writing – original draft, Writing – review & editing, Supervision, Project administration, Funding acquisition.

Declaration of competing interest

The authors declare that they have no known competing financial interests or personal relationships that could have appeared to influence the work reported in this paper.

Acknowledgements

The authors acknowledge the financial support from the Norwegian Research Council (research project FRIPRO-FRINATEK no. 324243 HELIOS), the Finnish Cultural Foundation, and Emil Aaltonen Foundation.

Appendix A. Supplementary data

Supplementary data to this article can be found online at https://doi.org/10.1016/j.renene.2023.119722.

References

[1] International Energy Agency, World Energy Outlook 2021, OECD, 2021, https://doi.org/10.1787/14fcb638-en.
[2] D. Gielen, F. Boshell, D. Saygin, M.D. Bazilian, N. Wagner, R. Gorini, The role of renewable energy in the global energy transformation, Energy Strategy Rev. 24 (2019) 38–50, https://doi.org/10.1016/J.ESR.2019.01.006.
[3] Intergovernmental Panel on Climate Change, Climate Change 2023: Synthesis Report. A Report of the Intergovernmental Panel on Climate Change. Contribution of Working Groups I, II and III to the Sixth Assessment Report of the Intergovernmental Panel on Climate Change IPCC, Geneva, Switzerland, 2023. https://www.ipcc.ch/report/ar6/syr/.
[4] S. Jouttijärvi, G. Lobaccaro, A. Kamppinen, K. Miettunen, Benefits of bifacial solar cells combined with low voltage power grids at high latitudes, Renew. Sustain. Energy Rev. 161 (2022), 112354, https://doi.org/10.1016/J.RSER.2022.112354.
[5] M.R. Khan, A. Hanna, X. Sun, M.A. Alam, Vertical bifacial solar farms: physics, design, and global optimization, Appl. Energy 206 (2017) 240–248, https://doi.org/10.1016/J.APENERGY.2017.08.042.
[6] International Energy Agency, IEA Statistics: Explore energy data by category, indicator, country or region, (n.d.). https://www.iea.or

g/data-and-statistics/data-browser?country=WORLD&fuel=Energy%5C supply&indicator=TESbySource (accessed March 21, 2022)..
[7] S. Guo, T.M. Walsh, M. Peters, Vertically mounted bifacial photovoltaic modules: a global analysis, Energy 61 (2013) 447–454, https://doi.org/10.1016/J.ENERGY.2013.08.040.
[8] C. Pike, E. Whitney, M. Wilber, J.S. Stein, Field performance of South-facing and East-West facing bifacial modules in the arctic, Energies 14 (2021), https://doi.org/10.3390/en14041210.
[9] J. Stein, Solar PV Performance and New Technologies in Northern Latitude Regions, 2018. https://www.osti.gov/biblio/1510188.
[10] R. Perez, R. Seals, A. Zelenka, P. Ineichen, Climatic evaluation of models that predict hourly direct irradiance from hourly global irradiance: prospects for performance improvements, Sol. Energy 44 (1990) 99–108, https://doi.org/10.1016/0038-092X(90)90071-J.
[11] M. Hofmann, G. Seckmeyer, Influence of various irradiance models and their combination on simulation results of photovoltaic systems, Energies 10 (2017), https://doi.org/10.3390/en10101495.
[12] C.D. Rodríguez-Gallegos, M. Bieri, O. Gandhi, J.P. Singh, T. Reindl, S.K. Panda, Monofacial vs bifacial Si-based PV modules: which one is more cost-effective? Sol. Energy 176 (2018) 412–438, https://doi.org/10.1016/J.SOLENER.2018.10.012.
[13] D. Araya-Muñoz, D. Carvajal, A. Sáez-Carreño, S. Bensaid, E. Soto-Márquez, Assessing the solar potential of roofs in Valparaíso (Chile), Energy Build. 69 (2014) 62–73, https://doi.org/10.1016/j.enbuild.2013.10.014.
[14] C.A. Gueymard, J.A. Ruiz-Arias, Extensive Worldwide Validation and Climate Sensitivity Analysis of Direct Irradiance Predictions from 1-min Global Irradiance, Pergamon, 2016, https://doi.org/10.1016/j.solener.2015.10.010.
[15] Z. Li, H. Xing, S. Zeng, J. Zhao, T. Wang, Comparison of anisotropic diffuse sky radiance models for irradiance estimation on building facades, Procedia Eng. 205 (2017) 779–786, https://doi.org/10.1016/J.PROENG.2017.10.010.
[16] A.R. Starke, L.F.L. Lemos, C.M. Barni, R.D. Machado, J.M. Cardemil, J. Boland, S. Colle, Assessing one-minute diffuse fraction models based on worldwide climate features, Renew. Energy 177 (2021) 700–714, https://doi.org/10.1016/J.RENENE.2021.05.108.
[17] B.L. Liu, R. Jordan, Daily Insolation on Surfaces Tilted towards Equator, 1961.
[18] R. Perez, R. Seals, P. Ineichen, R. Stewart, D. Menicucci, A new simplified version of the perez diffuse irradiance model for tilted surfaces, Sol. Energy 39 (1987) 221–231, https://doi.org/10.1016/S0038-092X(87)80031-2.
[19] D. Paul, G. De Michele, B. Najafi, S. Avesani, Benchmarking clear sky and transposition models for solar irradiance estimation on vertical planes to facilitate glazed facade design, Energy Build. 255 (2022), https://doi.org/10.1016/j.enbuild.2021.111622.
[20] C. Toledo, A.M. Gracia Amillo, G. Bardizza, J. Abad, A. Urbina, Evaluation of solar radiation transposition models for passive energy management and building integrated photovoltaics, Energies 13 (2020), https://doi.org/10.3390/en13030702.
[21] M. Hofmann, G. Seckmeyer, A new model for estimating the diffuse fraction of solar irradiance for photovoltaic system simulations, Energies 10 (2017), https://doi.org/10.3390/en10020248.
[22] M.P. Utrillas, J.A. Martinez-Lozano, Performance evaluation of several versions of the Perez tilted diffuse irradiance model, Sol. Energy 53 (1994) 155–162, https://doi.org/10.1016/0038-092X(94)90476-6.
[23] D. Yang, Estimating 1-min beam and diffuse irradiance from the global irradiance: a review and an extensive worldwide comparison of latest separation models at 126 stations, Renew. Sustain. Energy Rev. 159 (2022), 112195, https://doi.org/10.1016/J.RSER.2022.112195.
[24] D. Yang, Solar radiation on inclined surfaces: corrections and benchmarks, Sol. Energy 136 (2016) 288–302.
[25] M. Schroedter-Homscheidt, F. Azam, J. Betcke, N. Hanrieder, M. Lefèvre, L. Saboret, Y.M. Saint-Drenan, Surface solar irradiation retrieval from MSG/SEVIRI based on APOLLO Next Generation and HELIOSAT4 methods, Meteorol. Zeitschrift. 31 (2022) 455–476, https://doi.org/10.1127/metz/2022/1132.
[26] Z. Qu, A. Oumbe, P. Blanc, B. Espinar, G. Gesell, B. Gschwind, L. Klüser, M. Lefèvre, L. Saboret, M. Schroedter-Homscheidt, L. Wald, Fast radiative transfer parameterisation for assessing the surface solar irradiance: the Heliosat4 method, Meteorol. Zeitschrift. 26 (2017) 33–57, https://doi.org/10.1127/metz/2016/0781.
[27] B. Gschwind, L. Wald, P. Blanc, M. Lefèvre, M. Schroedter-Homscheidt, A. Arola, Improving the McClear model estimating the downwelling solar radiation at ground level in cloud-free conditions ? McClear?v3, Meteorol. Zeitschrift. 28 (2019) 147–163, https://doi.org/10.1127/metz/2019/0946.
[28] M. Lefèvre, A. Oumbe, P. Blanc, B. Espinar, B. Gschwind, Z. Qu, L. Wald, M. Schroedter-Homscheidt, C. Hoyer-Klick, A. Arola, A. Benedetti, J.W. Kaiser, J.-J. Morcrette, McClear: a new model estimating downwelling solar radiation at ground level in clear-sky conditions, Atmos. Meas. Tech. 6 (2013) 2403–2418, https://doi.org/10.5194/amt-6-2403-2013.
[29] C.A. Gueymard, J.A. Ruiz-Arias, Performance of separation models to predict direct irradiance at high frequency: validation over arid areas, in: EuroSun 2014, International Solar Energy Society, 2014.
[30] M. Manni, A. Nocente, M. Bellmann, G. Lobaccaro, Multi-stage validation of a solar irradiance model chain: an application at high latitudes, Sustainability 15 (2023), https://doi.org/10.3390/su15042938.
[31] W. Köppen, Versuch einer Klassifikation der Klimate, vorzugsweise nach ihren Beziehungen zur Pflanzenwelt, Geogr. Z. 6 (1900) 593–611. http://www.jstor.org/stable/27803924.
[32] J.A. Olseth, A. Skartveit, A probability density model for hourly total and beam irradiance on arbitrarily orientated planes, Sol. Energy 39 (1987) 343–351, https://doi.org/10.1016/S0038-092X(87)80020-8.
[33] A. Skartveit, J.A. Olseth, M.E. Tuft, An hourly diffuse fraction model with correction for variability and surface albedo, Sol. Energy 63 (1998) 173–183, https://doi.org/10.1016/S0038-092X(98)00067-X.
[34] D.G. Erbs, S.A. Klein, J.A. Duffie, Estimation of the diffuse radiation fraction for hourly, daily and monthly-average global radiation, Sol. Energy 28 (1982) 293–302, https://doi.org/10.1016/0038-092X(82)90302-4.
[35] R. Perez, P. Ineichen, E.L. Maxwell, R.D. Seals, A. Zelenka, Dynamic global-to-direct irradiance conversion models, ASHRAE Trans 98 (1992) 354–369.
[36] R. Perez, P. Ineichen, K. Moore, M. Kmiecik, C. Chain, R. George, F. Vignola, A new operational model for satellite-derived irradiances: description and validation, Sol. Energy 73 (2002) 307–317, https://doi.org/10.1016/S0038-092X(02)00122-6.
[37] T. Muneer, G.S. Saluja, Correlation between hourly diffuse and global solar irradiation for the UK, Build. Serv. Eng. Technol. 7 (1986) 37–43, https://doi.org/10.1177/014362448600700106.
[38] D.T. Reindl, W.A. Beckman, J.A. Duffie, Diffuse fraction correlations, Sol. Energy 45 (1990) 1–7, https://doi.org/10.1016/0038-092X(90)90060-.
[39] J.D. Mondol, Y.G. Yohanis, M. Smyth, B. Norton, Long-term validated simulation of a building integrated photovoltaic system, Sol. Energy 78 (2005) 163–176, https://doi.org/10.1016/j.solener.2004.04.021.
[40] J.D. Mondol, Y.G. Yohanis, B. Norton, Solar radiation modelling for the simulation of photovoltaic systems, Renew. Energy 33 (2008) 1109–1120, https://doi.org/10.1016/j.renene.2007.06.005.
[41] J.W. Spencer, A comparison of methods for estimating hourly diffuse solar radiation from global solar radiation, Sol. Energy 29 (1982) 19–32, https://doi.org/10.1016/0038-092X(82)90277-8.
[42] A. De Miguel, J. Bilbao, R. Aguiar, H. Kambezidis, E. Negro, Diffuse solar irradiation model evaluation in the North Mediterranean Belt area, Sol. Energy 70 (2001) 143–153, https://doi.org/10.1016/S0038-092X(00)00135-3.
[43] E. Paulescu, R. Blaga, A simple and reliable empirical model with two predictors for estimating 1-minute diffuse fraction, Sol. Energy 180 (2019) 75–84, https://doi.org/10.1016/J.SOLENER.2019.01.029.
[44] A.R. Starke, L.F.L. Lemos, J. Boland, J.M. Cardemil, S. Colle, Resolution of the cloud enhancement problem for one-minute diffuse radiation prediction, Renew. Energy 125 (2018) 472–484, https://doi.org/10.1016/J.RENENE.2018.02.107.
[45] N.A. Engerer, Minute resolution estimates of the diffuse fraction of global irradiance for southeastern Australia, Sol. Energy 116 (2015) 215–237, https://doi.org/10.1016/j.solener.2015.04.012.
[46] J.M. Bright, N.A. Engerer, Engerer2: global re-parameterisation, update, and validation of an irradiance separation model at different temporal resolutions, J. Renew. Sustain. Energy 11 (2019), 33701, https://doi.org/10.1063/1.5097014.
[47] D. Yang, J. Boland, Satellite-augmented diffuse solar radiation separation models, J. Renew. Sustain. Energy 11 (2019), 23705, https://doi.org/10.1063/1.5087463.
[48] D. Yang, Temporal-resolution cascade model for separation of 1-min beam and diffuse irradiance, J. Renew. Sustain. Energy 13 (2021), 56101, https://doi.org/10.1063/5.0067997.
[49] E.F.M. Abreu, P. Canhoto, M.J. Costa, Prediction of diffuse horizontal irradiance using a new climate zone model, Renew. Sustain. Energy Rev. 110 (2019) 28–42, https://doi.org/10.1016/J.RSER.2019.04.055.
[50] J.P. Every, L. Li, D.G. Dorrell, Köppen-Geiger climate classification adjustment of the BRL diffuse irradiation model for Australian locations, Renew. Energy 147 (2020) 2453–2469, https://doi.org/10.1016/J.RENENE.2019.09.114.
[51] B. Ridley, J. Boland, P. Lauret, Modelling of diffuse solar fraction with multiple predictors, Renew. Energy 35 (2010) 478–483, https://doi.org/10.1016/j.renene.2009.07.018.
[52] J.W. Bugler, The determination of hourly insolation on an inclined plane using a diffuse irradiance model based on hourly measured global horizontal insolation, Sol. Energy 19 (1977) 477–491, https://doi.org/10.1016/0038-092X(77)90103-7.
[53] J.E. Hay, D.C. McKay, Estimating solar irradiance on inclined surfaces: a review and assessment of methodologies, Int. J. Sol. Energy 3 (1985) 203–240, https://doi.org/10.1080/01425918508914395.
[54] R.C. Temps, K.L. Coulson, Solar radiation incident upon slopes of different orientations, Sol. Energy 19 (1977) 179–184, https://doi.org/10.1016/0038-092X(77)90056-1.
[55] T.M. Klucher, Evaluation of models to predict insolation on tilted surfaces, Sol. Energy 23 (1979) 111–114, https://doi.org/10.1016/0038-092X(79)90110-5.
[56] M.D. Steven, M.H. Unsworth, The diffuse solar irradiance of slopes under cloudless skies, Q. J. R. Meteorol. Soc. 105 (1979) 593–602, https://doi.org/10.1002/qj.49710544507.
[57] M.D. Steven, M.H. Unsworth, The angular distribution and interception of diffuse solar radiation below overcast skies, Q. J. R. Meteorol. Soc. 106 (1980) 57–61, https://doi.org/10.1002/qj.49710644705.
[58] J.E. Hay, J.A. Davies, Calculations of the solar radiation incident on an inclined surface, in: J.E. Hay, T.K. Won (Eds.), Proc. Of First Canadian Solar Radiation Data Workshop, 59. Ministry of Supply and Services, Canada., in: Proc. First Can. Sol. Radiat. Data Work., Toronto, 1980, pp. 59–72.
[59] J.E. Hay, Calculating solar radiation for inclined surfaces: practical approaches, Renew. Energy 3 (1993) 373–380, https://doi.org/10.1016/0960-1481(93)90104-O.
[60] C.J. Willmott, On the climatic optimization of the tilt and azimuth of flat-plate solar collectors, Sol. Energy 28 (1982) 205–216, https://doi.org/10.1016/0038-092X(82)90159-1.

[61] P.S. Koronakis, On the choice of the angle of tilt for south facing solar collectors in the Athens basin area, Sol. Energy 36 (1986) 217–225, https://doi.org/10.1016/0038-092X(86)90137-4.
[62] R. Perez, R. Seals, P. Ineichen, R. Stewart, D. Menicucci, A new simplified version of the perez diffuse irradiance model for tilted surfaces, Sol. Energy 39 (1987) 221–231, https://doi.org/10.1016/S0038-092X(87)80031-2.
[63] R. Perez, R. Stewart, R. Seals, T. Guertin, The Development and Verification of the Perez Diffuse Radiation Model, 1988, https://doi.org/10.2172/7024029.
[64] R. Perez, P. Ineichen, R. Seals, J. Michalsky, R. Stewart, Modeling daylight availability and irradiance components from direct and global irradiance, Sol. Energy 44 (1990) 271–289, https://doi.org/10.1016/0038-092X(90)90055-H.
[65] A. Skartveit, J. Asle Olseth, Modelling slope irradiance at high latitudes, Sol. Energy 36 (1986) 333–344, https://doi.org/10.1016/0038-092X(86)90151-9.
[66] C. Gueymard, An anisotropic solar irradiance model for tilted surfaces and its comparison with selected engineering algorithms, Sol. Energy 38 (1987) 367–386, https://doi.org/10.1016/0038-092X(87)90009-0.
[67] T. Muneer, Solar radiation model for Europe, Build. Serv. Eng. Technol. 11 (1990) 153–163, https://doi.org/10.1177/014362449001100405.
[68] D.T. Reindl, W.A. Beckman, J.A. Duffie, Evaluation of hourly tilted surface radiation models, Sol. Energy 45 (1990) 9–17, https://doi.org/10.1016/0038-092X(90)90061-G.
[69] F.J. Olmo, J. Vida, I. Foyo, Y. Castro-Diez, L. Alados-Arboledas, Prediction of global irradiance on inclined surfaces from horizontal global irradiance, Energy 24 (1999) 689–704, https://doi.org/10.1016/S0360-5442(99)00025-0.
[70] Y.Q. Tian, R.J. Davies-Colley, P. Gong, B.W. Thorrold, Estimating solar radiation on slopes of arbitrary aspect, Agric. For. Meteorol. 109 (2001) 67–74, https://doi.org/10.1016/S0168-1923(01)00245-3.
[71] V. Badescu, 3D isotropic approximation for solar diffuse irradiance on tilted surfaces, Renew. Energy 26 (2002) 221–233, https://doi.org/10.1016/S0960-1481(01)00123-9.
[72] C.A. Gueymard, Direct and indirect uncertainties in the prediction of tilted irradiance for solar engineering applications, Sol. Energy 83 (2009) 432–444, https://doi.org/10.1016/j.solener.2008.11.004.
[73] C.N. Long, Y. Shi, An automated quality assessment and control algorithm for surface radiation measurements, Open Atmos. Sci. J. 2 (2008) 23–37, https://doi.org/10.2174/1874282300802010023.
[74] M. Järvelä, K. Lappalainen, S. Valkealahti, Characteristics of the cloud enhancement phenomenon and PV power plants, Sol. Energy 196 (2020) 137–145, https://doi.org/10.1016/J.SOLENER.2019.11.090.
[75] C.A. Gueymard, A review of validation methodologies and statistical performance indicators for modeled solar radiation data: towards a better bankability of solar projects, Renew. Sustain. Energy Rev. 39 (2014) 1024–1034, https://doi.org/10.1016/j.rser.2014.07.117.
[76] B. Espinar, L. Ramírez, A. Drews, H.G. Beyer, L.F. Zarzalejo, J. Polo, L. Martín, Analysis of different comparison parameters applied to solar radiation data from satellite and German radiometric stations, Sol. Energy 83 (2009) 118–125, https://doi.org/10.1016/J.SOLENER.2008.07.009.
[77] C.A. Gueymard, Clear-sky irradiance predictions for solar resource mapping and large-scale applications: improved validation methodology and detailed performance analysis of 18 broadband radiative models, Sol. Energy 86 (2012) 2145–2169, https://doi.org/10.1016/j.solener.2011.11.011.
[78] G. Schwarz, Estimating the dimension of a model, Ann. Stat. 6 (1978) 461–464, https://doi.org/10.1214/aos/1176344136.
[79] H.K. Seidlitz, S. Thiel, A. Krins, H. Mayer, Solar radiation at the Earth's surface, Compr. Ser. Photosciences. 3 (2001) 705–738, https://doi.org/10.1016/S1568-461X(01)80071-5.
[80] E. Lorenz, P. Guthke, A. Dittmann, N. Holland, W. Herzberg, S. Karalus, B. Müller, C. Braun, W. Heydenreich, Y.M. Saint-Drenan, High resolution measurement network of global horizontal and tilted solar irradiance in southern Germany with a new quality control scheme, Sol. Energy 231 (2022) 593–606, https://doi.org/10.1016/J.SOLENER.2021.11.023.
[81] M. Manni, A. Nocente, G. Kong, K. Skeie, H. Fan, G. Lobaccaro, Solar energy digitalization at high latitudes: a model chain combining solar irradiation models, a LiDAR scanner, and high-detail 3D building model, Front. Energy Res. 10 (2022), https://doi.org/10.3389/fenrg.2022.1082092.